Solar RRL

RESEARCH ARTICLE

Silver Substitutional Doping to Enhance the Photoelectrochemical Properties of $BiFeO_3$ Photocathodes via Promoting Photon Absorption and Bulk Carrier Transport

Jingang Guo | Yudong Han | Ruojie Liu | Jiahao Yang | Yiqi Wang | Haowei Yu | Senhao Wang | Donglin Jia | Jianan Gu | Yanhong Wang | Yanlong Lv | Xiaojun Lv | Xin Sun | Meicheng Li

State Key Laboratory of Alternate Electrical Power System with Renewable Energy Sources, School of New Energy, North China Electric Power University, Beijing, China

Correspondence: Xin Sun (xsun@ncepu.edu.cn) | Meicheng Li (mcli@ncepu.edu.cn)

Received: 16 November 2025 | **Revised:** 4 December 2025 | **Accepted:** 16 December 2025

Keywords: Ag doping | $BiFeO_3$ | photocathode | photoelectrochemical properties

ABSTRACT

Perovskite-type $BiFeO_3$ (BFO) has been considered as a promising candidate for photoelectrochemical cells due to its suitable band alignment, robust ferroelectric behavior, and good chemical stability. However, the photoelectrochemical performance of BFO is limited by poor photon utilization and severe charge carrier losses. In this work, the Bi^{3+} sites of p-type BFO thin films are substitutionally doped by Ag^{+} to improve their photon absorption and bulk carrier transport, thereby enhancing photoelectrochemical responses. The results show that Ag doping reduces the bandgap of BFO photocathodes, broadening spectral absorption. Furthermore, Ag doping regulates the growth of BFO grains to form the films composed of single-layer grains, which effectively reduces bulk charge recombination associated with grain boundaries. Also, the bulk charge transport is further improved by the increase in majority carrier density induced by Ag doping. As a result, the photocurrent density of 6% Ag-doped BFO photocathodes reaches $-0.88\ mA{\cdot}cm^{-2}$ at 0.5 V vs RHE in O_2-saturated electrolytes, which is more than 5 times higher than that of pristine BFO photocathodes. This study lays a solid foundation for facilitating efficient solar fuel generation based on BFO photocathodes.

1 | Introduction

With the development of society, the increasing consumption of fossil fuels has triggered energy crises and environmental pollution. Solar energy, as a clean, abundant, and widely accessible resource, has driven intensive research into its efficient conversion and storage [1]. Photoelectrochemical (PEC) solar fuel generation is one of the important technologies for solar energy utilization [2, 3]. Under the irradiation, the semiconductor photoelectrode produces electron and hole pairs. These photogenerated charge carriers participate in the redox reactions at the semiconductor-electrolyte interfaces, driving a series of important reactions, such as water splitting, organic pollutant degradation, and carbon dioxide reduction [4–6]. Metal oxides (e.g., Fe_2O_3, Cu_2O, and $BiVO_4$) are commonly used to fabricate the photoelectrode due to their high stability in aqueous solutions, low cost and facile processing [7–11].

Bismuth ferrite, $BiFeO_3$ (BFO), is an interesting and promising perovskite oxide in the PEC field [12–17]. According to different synthesis methods, it can present both n-type and p-type conductivity, as well as a broad range of bandgap values from 2.2 to 2.8 eV [18–21]. Furthermore, the ferroelectric properties of BFO allow for more flexible and versatile regulation of its PEC behaviors [22–24]. However, intrinsic BFO photoelectrodes suffer from severe photogenerated carrier recombination due to

low carrier mobility, which seriously restricts its quantum efficiency for solar fuel generation [14, 17, 19]. In this case, researchers have proposed various strategies to enhance their performance. For example, diverse functional materials, including Au, rGO, C1+PDI, g-C_3N_4, $BiFe_{0.95}Mn_{0.05}O_3$, and $LaNiO_3$, have been composited with BFO, thereby improving carrier separation and transport efficiency [25–30]. It has also been shown that regulating BFO composition, including the Bi:Fe ratio and intrinsic defects, can significantly improve its PEC properties [31–33], where the gradient defect modulations leads to a remarkable photocurrent of $-1.02\,mA{\cdot}cm^{-2}$ at 0.5 V vs RHE [33]. In addition, atomic doping or substitution has been demonstrated as an effective approach to enhance the PEC performance of BFO. Yuan et al. reported that alkali metal (Na) doping greatly strengthens the p-type characteristics of BFO, boosting its photocurrent responses for O_2 reduction [34]. Interestingly, other studies mainly used lanthanide rare earth metal ions with the same valence as Bi^{3+}, including Sm^{3+} and Nd^{3+}, for doping BFO photocathodes [17, 35]. Previous studies have demonstrated that dopants with valence states lower than that of the host element at the substitutional site can induce an intrinsic charge compensation mechanism, thereby modifying the electronic structure of p-type materials to a state more favorable for enhancing their PEC performance [36, 37].

In this work, we use Ag, a transition metal that predominantly exhibits $a+1$ valence state, to substitutionally dope the Bi site of BFO thin-film photocathode, which increases photocurrent density by more than 5 times in O_2-saturated 0.1 M Na_2SO_4 aqueous solutions at pH 12. The pristine and Ag-doped BFO films were prepared by sol–gel methods, both exhibiting obvious p-type conductivity. X-ray diffraction (XRD) and X-ray photoemission spectroscopy (XPS) analysis confirm the successful substitutional doping of Ag^+ into BFO films, along with an evident charge compensation in the film. Optical characterization shows that Ag doping reduces the bandgap of BFO, which increases the light absorption capacity. In addition, scanning electron microscope (SEM) images reveal that Ag-doped BFO films exhibit larger grain sizes and fewer grain boundaries, promoting the photogenerated carrier transport. Also, the bulk charge carrier mobility of BFO films is further enhanced by the increase in majority carrier density upon Ag doping, as verified by Mott–Schottky plots. This work demonstrates an effective method for enhancing the PEC behavior of p-type BFO.

2 | Result and Discussion

Figure 1 shows the XRD patterns with Rietveld refinement of pristine and Ag-doped BFO films deposited on the glass side of F-doped SnO_2 (FTO) substrates. All diffraction peaks correspond to the BFO phase with the R3c space group, consistent with the standard reference pattern. The Rietveld refinement results in Table S1 show that Ag doping leads to slight decrease in lattice volume. This phenomenon can be rationalized by comparing the ionic radius of different cations. The ionic radius of Ag^+ (1.09 Å) is larger than that of Bi^{3+} (1.03 Å). Thus, with the increase in the Ag doping level, the average ionic radius at the A-site of BFO expands, resulting in the enlarged lattice parameters. However, Ag doping is accompanied by a partial oxidation of Fe^{3+} to Fe^{4+}, as shown later. This triggers the contraction of the lattice volume, since the ionic radius of high-spin Fe^{3+} (0.645 Å) is larger than that of Fe^{4+} (0.585 Å). The competition between the A-site expansion and the B-site contraction eventually leads to subtle changes in the lattice parameters. Indeed, Sun et al. also observed this phenomenon in Ba-substituted $LaFeO_3$ thin films [37].

In order to study the evolution of the oxidation state of elements in the films upon Ag doping, XPS measurements were carried out at room temperature. Figure 2a,b show the Gaussian-fitted spectra of various elements of pristine and 6% Ag-doped BFO films, respectively. The data show the Bi 4f signals remain unchanged before and after Ag doping. Two peaks at 158.9 and 164.2 eV correspond to Bi $4f_{7/2}$ and Bi $4f_{5/2}$, respectively, indicating Bi is in a trivalent state in the films [38]. Similarly, the characteristic peak positions of the Fe 2p photoemission also suggest that Fe in both pristine and Ag-doped films predominantly exists in the +3 oxidation state [39, 40]. According to previous studies, the Fe 2p predominant signals can be deconvoluted into three components (Fe^{2+}, Fe^{3+}, and Fe^{4+}) [41, 42]. The content of the various Fe species (Table S2) indicates that Ag doping results in an increase in the valence state of Fe, for instance, the Fe^{4+} content in 6% Ag-doped BFO films is 1.75 times that of pristine BFO films. This evolution occurs because the doping of Ag^+ induces a change in Fe from lower to higher oxidation states to maintain the charge neutrality [36, 37, 42]. As for the O 1s spectra in Figure 2, the main peak at around 529.0 eV corresponds to the oxygen in the crystal lattice (O_L) [40]. The other species can be assigned to surface hydroxyl (-OH) and undercoordinated

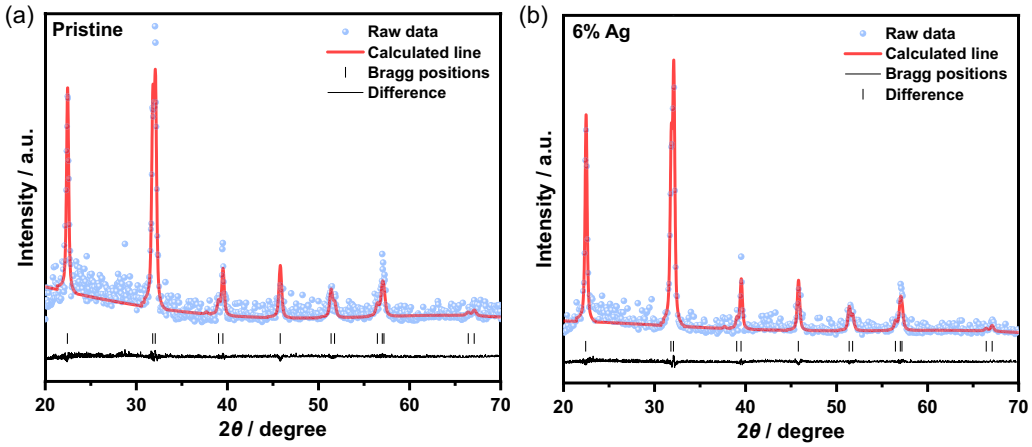

FIGURE 1 | XRD patterns with quantitative Rietveld refinement: (a) pristine BFO films and (b) 6% Ag-doped BFO films.

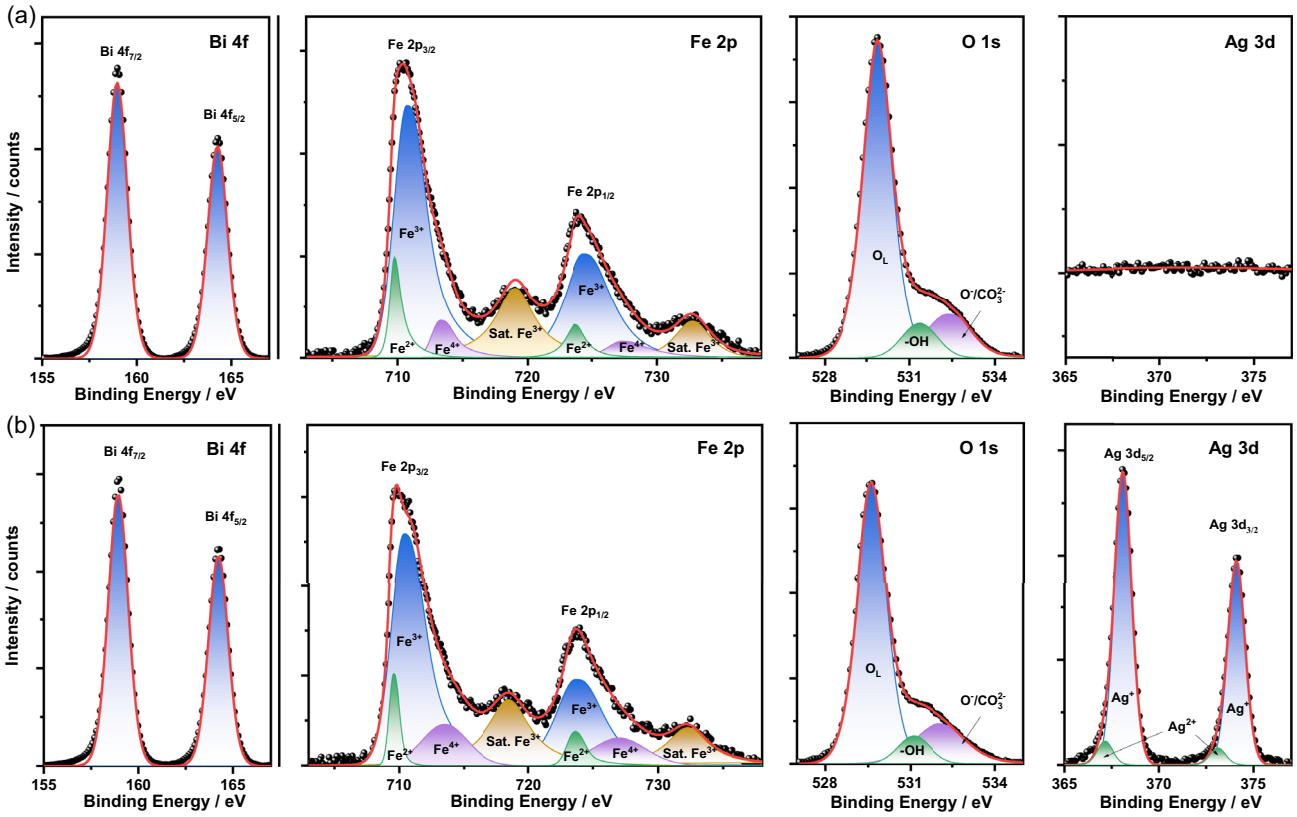

FIGURE 2 | Deconvolution of the high-resolution XPS signals of Bi 4f, Fe 2p, O 1s, and Ag 3d core-level: (a) pristine BFO films and (b) 6% Ag-doped BFO films.

oxygen/carbonylated compounds (O^{-}/CO_3^{2-}) [40, 42]. We have also observed that Ag doping affects the O 1s signals, which can be associated with the change in Fe–O bond strength and the generation of oxygen vacancies [40, 43]. The Ag 3d photoemission of 6% Ag-doped BFO films exhibits double peaks at 368.1/374.1 and 367.1/373.2 eV, corresponding to Ag^{+} and Ag^{2+}, respectively [44]. This deconvolution results confirm that Ag is mainly in the +1 oxidation state in the films.

Figure 3 displays the role of Ag doping on the morphology of BFO films. As shown in Figure 3a, the as-received pristine BFO films possess flat surfaces with small grains. Upon substitutional doping of 6% Ag into the film (Figure 3b), the BFO grains

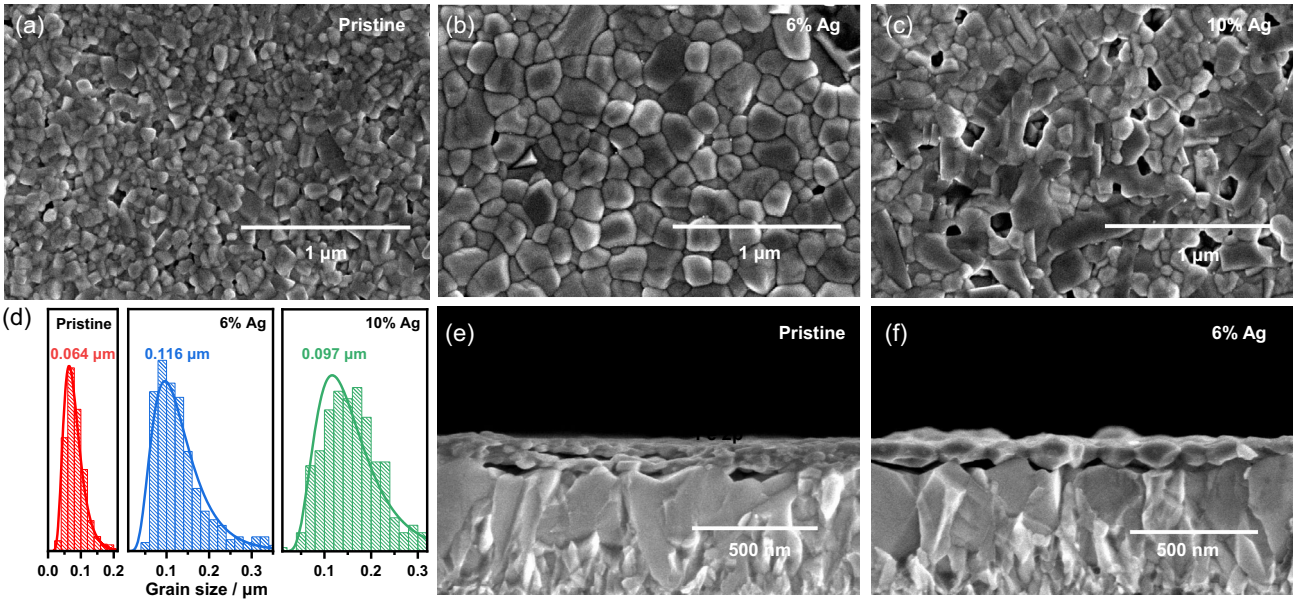

FIGURE 3 | (a–c) Top view SEM images of pristine and Ag-doped BFO films. (d) Corresponding grain size distribution statistics. (e,f) Cross-sectional SEM images of pristine and 6% Ag-doped BFO films.

exhibit a substantial increase. However, excessive Ag doping (e.g., 10% Ag content in Figure 3c) not only results in reduced grain sizes but also induces the formation of pinholes on the surfaces. Figure 3d shows the grain size distribution statistics, clearly revealing the trend of BFO grain size with increasing Ag doping level. The cross-sectional SEM images in Figure 3e,f reveal that 6% Ag doping increases the film thickness from 120 to 124 nm. This slight thickness variation is generally considered to have a small impact on the performance of BFO films, particularly in comparison to other significant changes induced by Ag doping discussed later, though the increased film thickness can enhance light absorption. It is worth noting that the thickness of 6% Ag-doped films is close to its grain size, which means the films consist of only a single layer of grains. This remarkable change can effectively reduce grain boundaries, thereby promoting charge carrier transport in the bulk [45, 46].

The optical properties of pristine and 6% Ag-doped BFO films were analyzed by UV-Vis absorption spectra. Their corresponding Tauc plots are shown in Figure 4a. The data show that pristine BFO films possess a direct optical bandgap of 2.66 eV, which is consistent with the previously reported value estimated from BFO films prepared by the sol–gel method [47]. After 6% Ag doping, the bandgap decreases to 2.54 eV, effectively broadening the spectral absorption range. Mott–Schottky plots were used to analyze the electronic properties of the BFO films. The negative slopes of the linear region indicate the p-type conductivity of both pristine and Ag-doped BFO films. The majority carrier density (N_a) of BFO films calculated from the slope demonstrates an enhancement from 4.25×10^{17} to 7.05×10^{17} cm^{-3} after Ag doping. Although the trend of N_a variation is clear, the calculated values are affected by multiple factors, including effective surface areas, dielectric constant, and the complex contribution of Helmholtz layers [4, 48]. The valence-band spectra of BFO films (Figure S1) acquired from XPS measurement are further analyzed to compare N_a prior to and after Ag doping. The data show that for Ag-doped BFO films, their Fermi level position is closer to the valence band, accompanied by a sharp increase in photoemission intensity, which further confirms that Ag doping enhances N_a [4, 37]. This enhancement originates from the increased valence state of Fe (Figure 2) upon Ag doping, generating more holes in BFO films. In addition, the flat band potential can be estimated from the x-intercept of the linear region. It can be seen that 6% Ag doping enables the flat band potential of BFO films to shift from 1.79 to 1.58 V vs RHE. Combining the flat band potential and bandgap energy, it can be observed that Ag doping can shift the conduction band minimum of BFO films upward, further enhancing the thermodynamic feasibility of BFO for PEC reactions such as the hydrogen evolution reaction.

Figure 5a displays the linear sweep voltammetry (LSV) of various BFO films for O_2 reduction under chopped AM 1.5G illumination in 0.1 M Na_2SO_4 electrolytes at pH 12. As oxygen is a strong electron scavenger, charge carrier recombination at the BFO-electrolyte surface is effectively suppressed, exhibiting significant photocurrent responses. The data also demonstrate that Ag doping greatly enhances the photocurrent density. With an increase in doping concentration, the photocurrent initially rises and then decreases, as shown in Figure 5b. Remarkably, 6% Ag doping enables BFO films to exhibit a photocurrent density of -0.88 $mA \cdot cm^{-2}$ at 0.5 V vs RHE, which is more than 5 times that of pristine BFO films. It should be noted that the photocurrent density can be further improved by using established performance-enhancing strategies [30–33], since the as-prepared pristine BFO films exhibit relatively low photocurrent density compared with some other reported values (as shown in Table S3). The external quantum efficiency (EQE) spectra of pristine and 6% Ag-doped BFO films for the oxygen reduction rection are plotted in Figure 5c, revealing that Ag doping boosts the photoresponses across the whole spectral region. The Tauc representations in Figure S2 acquired from the EQE spectra are highly consistent with those from optical analysis (Figure 4a), which further confirms that Ag doping can increase the photon absorption of BFO films. Figure S3 provides a preliminary assessment of the PEC stability of BFO films before and after doping with 6% Ag, indicating that low-concentration Ag doping does not compromise the ability of BFO films to exhibit stable photocurrent responses.

Figure 5d shows the photocurrent density of pristine and Ag-doped BFO films as a function of the potential for PEC water splitting under the same illumination conditions and electrolytes as Figure 5a. The photocurrent responses demonstrate sharp spikes, which suggests surface charge carrier recombination occurring in BFO films during the hydrogen evolution [49, 50]. This phenomenon is very common in pristine photoelectrodes, since the surfaces of most absorbers lack catalytic activity for water splitting [51]. Although the photocurrent density for the hydrogen evoluiton remains considerably lower than that for

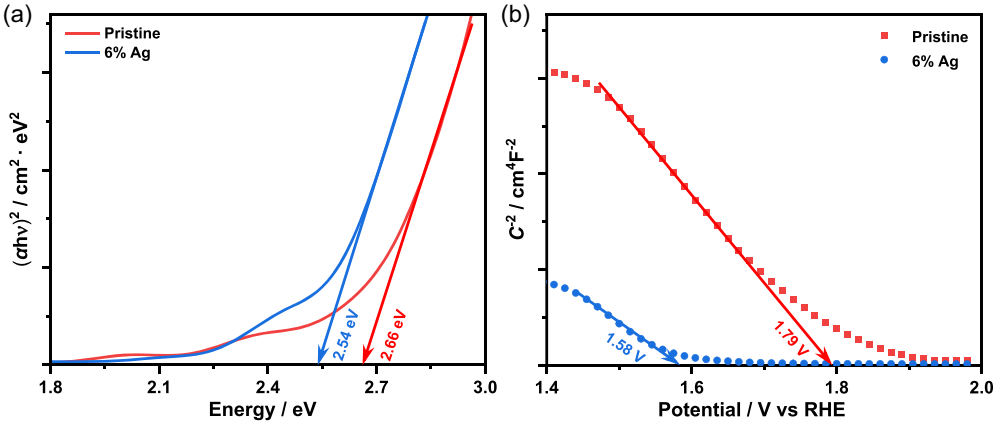

FIGURE 4 | Optical and electronic properties of pristine and 6% Ag-doped BFO films: (a) Tauc plots and (b) Mott–Schottky plots.

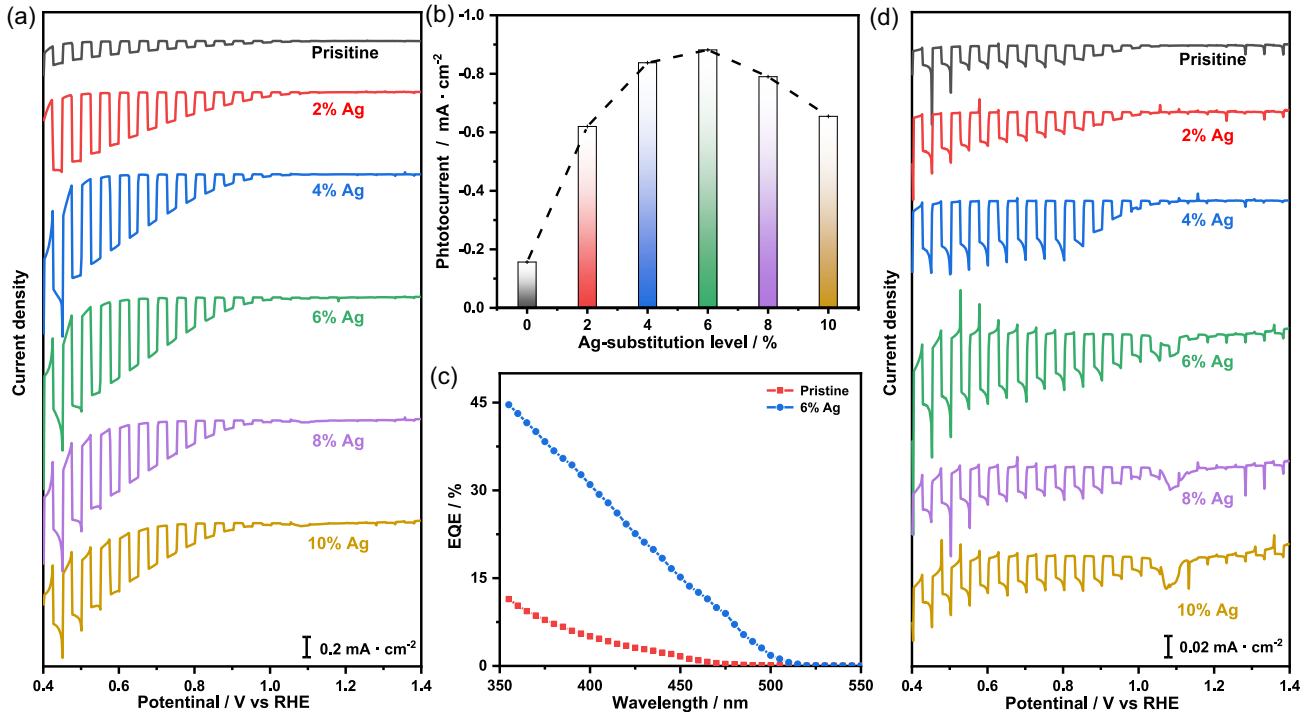

FIGURE 5 | PEC responses of BFO films with different Ag doping levels: (a) LSV curves in O_2-purged aqueous solutions, (b) corresponding photocurrent density 0.5 V vs RHE, (c) corresponding EQE spectra, and (d) LSV curves in Ar-saturated aqueous solutions.

the oxygen reduction, significantly enhanced quasi-steady-state photocurrent density is still observed in Ag-doped BFO films compared to pristine BFO films during the PEC water splitting. It can also be seen that when Ag doping concentrations exceed 4%, the dark current responses exhibit pseudocapacitive behaviors (distinct shoulders in the range of 1.0–1.1 V vs RHE), which is linked to the sub-bandgap states generated by the promoted hybridization between Fe 3d and O 1s states upon Ag doping [37, 41]. These sub-bandgap states usually act as carrier recombination centers. Consequently, this constitutes one primary factor for the reduction in the photocurrent density in highly Ag-doped BFO films.

The enhancement of the PEC performance of BFO films upon Ag doping stems from multiple aspects, as summarized in Figure 6. First, Ag doping narrows the bandgap of BFO films, enhancing the absorption of low-energy photons. Second, Ag doping enlarges the BFO grains to a size approaching the film thickness, thereby yielding polycrystalline films composed of a single layer of grains. This structure enables Ag-doped BFO films to possess fewer grain boundaries, effectively suppressing carrier recombination during

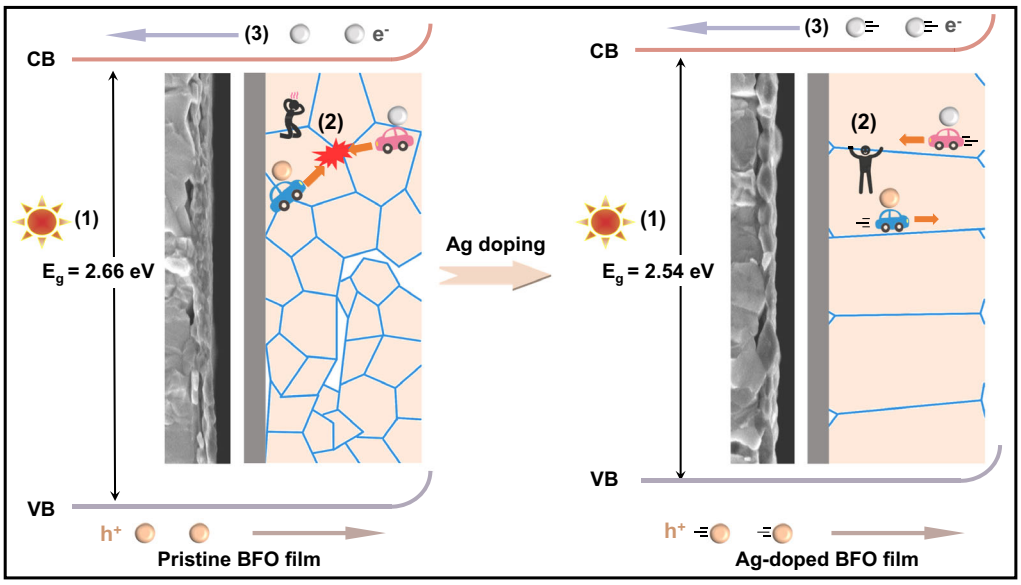

FIGURE 6 | Schematic of Ag doping for improving PEC performance of BFO films.

bulk transport. Third, the increase in the Fe valence state, induced by Ag doping, raises the majority carrier density in the p-type BFO films, enhancing the mobility of photogenerated charge carriers. This, in turn, further improves the bulk carrier transfer efficiency.

3 | Conclusions

The pristine and Ag-doped BFO thin films were successfully fabricated via sol–gel methods, yielding high-quality photocathodes with phase purity, good crystallinity, as well as compact and uniform surface morphology. Our findings show that partial Ag^+ doping into BFO films can greatly enhance their photon absorption and bulk carrier transport by regulating bandgap, microstructure, and carrier density. As a result, Ag doping significantly improves the PEC performance of BFO films. Remarkably, 6% Ag doping enables the photocurrent density of BFO films for the oxygen reduction reaction to increase from −0.16 to −0.88 $mA{\cdot}cm^{-2}$ at 0.5 V vs RHE. Furthermore, Ag doping also enhances the photoresponses of BFO films during the water splitting process across the entire potential window, though their poor surface reaction kinetics for the hydrogen evolution reaction result in low photocurrent density. The mechanism of PEC performance enhancement via Ag doping proposed in this study can provide important insights for clarifying the effects of other dopants on the PEC behavior of photoelectrodes.

4 | Experimental Section

4.1 | Thin-Film Preparation

A citric acid-assisted sol–gel method was used to fabricate various BFO films. First, precursor solutions were prepared by dissolving 0.5 M $Bi(NO_3)_3{\cdot}5H_2O$ in an ethanol/ethylene glycol mixture (1:1 v/v), which was then mixed with 0.5 M $Fe(NO_3)_3{\cdot}9H_2O$ ethanol solutions and 1 M citric acid ethanol solutions under stirring for 18 h to ensure chelation homogeneity. Second, the resulting precursors were spin-coated onto FTO substrates at 3000 rpm for 30 s, followed by a two-stage thermal treatment (predrying at 100°C on a hotplate for 10 min and annealing at 400°C in a muffle furnace for 1 h). After repeating the coating-annealing cycle three times, the films were calcinated at 600°C in a muffle furnace for 3 h, generating prisitne BFO films. As for Ag-doped BFO films, they were prepared by stoichiometrically replacing $Bi(NO_3)_3{\cdot}5H_2O$ with $AgNO_3$, while strictly maintaining all other experimental parameters identical to those of the pristine BFO protocol.

4.2 | Photoelectrochemical Characterizations

All PEC measurements were conducted with an IviumStat potentiostat using a three-electrode system (BFO working electrode, carbon counter electrode, and Ag/AgCl reference electrode) in Ar-saturated or O_2-saturated 0.1 M Na_2SO_4 electrolytes. The pH of the electrolyte was adjusted to 12 using an aqueous solution of concentrated sodium hydroxide. All potentials reported in this work have been converted to against the reversible hydrogen electrode (RHE) according to the Nernst equation. LSV curves were performed at a scan rate of 5 $mV{\cdot}s^{-1}$ from positive to negative potentials. The standard AM 1.5G solar illumination (100 $mW{\cdot}cm^{-2}$) was simulated by a 300 W xenon lamp system equipped with an AM 1.5G filter. The EQE spectra were measured using the xenon lamp coupled with a monochromator. Other characterization methods are described in the Supporting Information.

Acknowledgments

This work was supported partially by the National Natural Science Foundation of China (52302250, 62474064, and 52402255), the Hebei Natural Science Foundation (B2024502013), the Beijing Natural Science Foundation (26JL001), the 2022 Strategic Research Key Project of Science and Technology Commission of the Ministry of Education, the China Postdoctoral Science Foundation (2022M721129), the Fundamental Research Funds for the Central Universities (2025MS046, 2024MS037, and 2025JC006), and the NCEPU "Double First-Class" Program.

Funding

This study was supported by the National Natural Science Foundation of China (52302250, 62474064, and 52402255), the Hebei Natural Science Foundation (B2024502013), the Beijing Natural Science Foundation (26JL001), the 2022 Strategic Research Key Project of Science and Technology Commission of the Ministry of Education, the China Postdoctoral Science Foundation (2022M721129), the Fundamental Research Funds for the Central Universities (2025MS046, 2024MS037, and 2025JC006), and the NCEPU "Double First-Class" Program.

Conflicts of Interest

The authors declare no conflicts of interest.

Data Availability Statement

The data that support the findings of this study are available from the corresponding author upon reasonable request.

References

1. N. S. Lewis, "Research Opportunities to Advance Solar Energy Utilization," *Science* 351, no. 6271 (2016): aad1920, https://doi.org/10.1126/science.aad1920.

2. Z. G. Schichtl, O. Q. Carvalho, J. Tan, et al., "Chemistry of Materials Underpinning Photoelectrochemical Solar Fuel Production," *Chemical Reviews* 125, no. 10 (2025): 4768–4839, https://doi.org/10.1021/acs.chemrev.4c00258.

3. K. Sivula and R. Van De Krol, "Semiconducting Materials for Photoelectrochemical Energy Conversion," *Nature Reviews Materials* 1, no. 2 (2016): 1–16, https://doi.org/10.1038/natrevmats.2015.10.

4. X. Sun, M. Wang, H. Li, et al., "Pristine $GaFeO_3$ Photoanodes with Surface Charge Transfer Efficiency of Almost Unity at 1.23 V for Photoelectrochemical Water Splitting," *Advanced Science* 10, no. 8 (2023): 2205907, https://doi.org/10.1002/advs.202205907.

5. B. Liu, T. Wang, S. Wang, et al., "Back-Illuminated Photoelectrochemical Flow Cell for Efficient CO_2 Reduction," *Nature Communications* 13, no. 1 (2022): 7111, https://doi.org/10.1038/s41467-022-34926-x.

6. S. Liu, Q. Xing, Y. Chen, et al., "Photoelectrochemical Degradation of Organic Pollutants Using BiOBr Anode Coupled with Simultaneous CO_2 Reduction to Liquid Fuels via CuO Cathode," *ACS Sustainable Chemistry & Engineering* 7, no. 1 (2019): 1250–1259, https://doi.org/10.1021/acssuschemeng.8b04917.

7. H. Zhang, D. Li, W. J. Byun, et al., "Gradient Tantalum-Doped Hematite Homojunction Photoanode Improves Both Photocurrents and Turn-on Voltage for Solar Water Splitting," *Nature Communications* 11, no. 1 (2020): 4622, https://doi.org/10.1038/s41467-020-18484-8.

8. L. Pan, J. H. Kim, M. T. Mayer, et al., "Boosting the Performance of Cu_2O Photocathodes for Unassisted Solar Water Splitting Devices," *Nature Catalysis* 1, no. 6 (2018): 412–420, https://doi.org/10.1038/s41929-018-0077-6.

9. M. I. Díez-García and R. Gómez, "Progress in Ternary Metal Oxides as Photocathodes for Water Splitting Cells: Optimization Strategies," *Solar RRL* 6, no. 4 (2022): 2100871, https://doi.org/10.1002/solr.202100871.

10. D. K. Lee, D. Lee, M. A. Lumley, and K. S. Choi, "Progress on Ternary Oxide-Based Photoanodes for use in Photoelectrochemical Cells for Solar Water Splitting," *Chemical Society Reviews* 48, no. 7 (2019): 2126–2157, https://doi.org/10.1039/c8cs00761f.

11. M. Xiao, B. Luo, Z. Wang, S. Wang, and L. Wang, "Recent Advances of Metal-Oxide Photoanodes: Engineering of Charge Separation and Transportation toward Efficient Solar Water Splitting," *Solar RRL* 4, no. 8 (2020): 1900509, https://doi.org/10.1002/solr.201900509.

12. P. Yilmaz, D. Yeo, H. Chang, L. Loh, and S. Dunn, "Perovskite $BiFeO_3$ Thin Film Photocathode Performance with Visible Light Activity," *Nanotechnology* 27, no. 34 (2016): 345402, https://doi.org/10.1088/0957-4484/27/34/345402.

13. M. Chu, N. Chanlek, C. Chen, et al., "Coupled Ferroelectric-Photoelectrochemical in Water Reduction Over $BiFeO_3$ Thin Film Heterostructure Modulated by Rare-Earth Doping," *Advanced Functional Materials* (2025): e16031, https://doi.org/10.1002/adfm.202516031.

14. G. Liu, S. K. Karuturi, H. Chen, et al., "Enhancement of the Photoelectrochemical Water Splitting by Perovskite $BiFeO_3$ via Interfacial Engineering," *Solar Energy* 202 (2020): 198–203, https://doi.org/10.1016/j.solener.2020.03.117.

15. X. Li, Z. Wang, W. Ji, et al., "Polarization Alignment in Polycrystalline $BiFeO_3$ Photoelectrodes for Tunable Band Bending," *ACS Nano* 17, no. 22 (2023): 22944–22951, https://doi.org/10.1021/acsnano.3c08081.

16. J. Song, T. L. Kim, J. Lee, et al., "Domain-Engineered $BiFeO_3$ Thin-Film Photoanodes for Highly Enhanced Ferroelectric Solar Water Splitting," *Nano Research* 11, no. 2 (2018): 642–655, https://doi.org/10.1007/s12274-017-1669-1.

17. S. Man, X. Leng, J. Bai, et al., "Enhancement of Photoelectrochemical Performance of $BiFeO_3$ by Sm^{3+} Doping," *Ceramics International* 49, no. 7 (2023): 10255–10264, https://doi.org/10.1016/j.ceramint.2022.11.205.

18. A. Radmilovic, T. J. Smart, Y. Ping, and K. S. Choi, "Combined Experimental and Theoretical Investigations of n-Type $BiFeO_3$ for Use as a Photoanode in a Photoelectrochemical Cell," *Chemistry of Materials* 32, no. 7 (2020): 3262–3270, https://doi.org/10.1021/acs.chemmater.0c00545.

19. Q. Yu, M. Yang, X. Luo, et al., "Improving Photoelectrochemical Water Oxidation Activity of $BiFeO_3$ Photoanode via Surface Passivation," *Applied Physics Letters* 119, no. 1 (2021): 013903, https://doi.org/10.1063/5.0047079.

20. J. He, Y. Liu, J. Qu, et al., "The Ferroelectric Effects of Rhombohedral and Tetragonal $BiFeO_3$ in Photoelectrochemical Water Splitting," *Journal of Physical Chemistry Letters* 15, no. 23 (2024): 6031–6037, https://doi.org/10.1021/acs.jpclett.4c01245.

21. D. Sando, C. Carrétéro, M. N. Grisolia, et al., "Revisiting the Optical Band Gap in Epitaxial $BiFeO_3$ Thin Films," *Advanced Optical Materials* 6, no. 2 (2018): 1700836, https://doi.org/10.1002/adom.201700836.

22. J. H. Shah, H. Ye, Y. Liu, et al., "Exploration of the Intrinsic Factors Limiting the Photocurrent Density in Ferroelectric $BiFeO_3$ Thin Film," *Journal of Materials Chemistry A* 8, no. 14 (2020): 6863–6873, https://doi.org/10.1039/d0ta00955e.

23. M. Li, A. Kursumovic, X. Qi, and J. L. MacManus-Driscoll, "Rapid Epitaxial Growth of Magnetoelectric Thick $BiFeO_3$ Films by Hybrid Liquid-Phase Epitaxy," *Journal of Crystal Growth* 293, no. 1 (2006): 128–135, https://doi.org/10.1016/j.jcrysgro.2006.04.108.

24. M. Li and J. L. MacManus-Driscoll, "Phase Stability, Oxygen Nonstoichiometry and Magnetic Properties of $BiFeO_{3-\delta}$," *Applied Physics Letters* 87, no. 25 (2005): 252510, https://doi.org/10.1063/1.2150249.

25. Y. Huang, W. Chang, C. Van, et al., "Tunable Photoelectrochemical Performance of Au/$BiFeO_3$ Heterostructure," *Nanoscale* 8, no. 34 (2016): 15795–15801, https://doi.org/10.1039/c6nr04997d.

26. Y. Ren, F. Nan, L. You, et al., "Enhanced Photoelectrochemical Performance in Reduced Graphene Oxide/$BiFeO_3$ Heterostructures," *Small* 13, no. 16 (2017): 1603457, https://doi.org/10.1002/smll.201603457.

27. M. Yan, Y. Li, C. Liu, et al., "Promoting H_2 Generation of $BiFeO_3$ Photocathodes by a Catalyst-Sensitizer Dyad Linked with $Sn(dipicolinate)_2$," *Chemical Communications* 60, no. 42 (2024): 5506–5509, https://doi.org/10.1039/d4cc01091d.

28. S. Wang, F. Nan, Y. Zhou, et al., "Enhanced Photoelectrochemical Performance in $BiFeO_3$/g-C_3N_4 p-n Heterojunction Photocathodes with Ferroelectric Polarization," *Journal of Applied Physics* 128, no. 15 (2020): 154101, https://doi.org/10.1063/5.0018856.

29. H. Xu, H. Wang, J. Shi, Y. Lin, and C. Nan, "Photoelectrochemical Performance Observed in Mn-Doped $BiFeO_3$ Heterostructured Thin Films," *Nanomaterials* 6, no. 11 (2016): 215, https://doi.org/10.3390/nano6110215.

30. Z. Zhang, B. Tan, W. Ma, et al., "$BiFeO_3$ Photocathodes for Efficient H_2O_2 Production via Charge Carrier Dynamics Engineering," *Materials Horizons* 9, no. 7 (2022): 1999–2006, https://doi.org/10.1039/d2mh00201a.

31. N. P. Prasad, M. Rohnke, M. A. Verheijen, et al., "Role of Excess Bi on the Properties and Performance of $BiFeO_3$ Thin-Film Photocathodes," *ACS Applied Energy Materials* 6, no. 24 (2023): 12237–12248, https://doi.org/10.1021/acsaem.3c01926.

32. Z. Nie, X. Yan, B. Zhang, et al., "Surface Defects Engineering of $BiFeO_3$ Films for Improved Photoelectrochemical Water Oxidation," *Ceramics International* 48, no. 24 (2022): 36279–36286, https://doi.org/10.1016/j.ceramint.2022.08.187.

33. B. Tan, A. M. Reyes, E. Menéndez-Proupin, et al., "Full-Space Potential Gradient Driven Charge Migration inside $BiFeO_3$ Photocathode," *ACS Energy Letters* 7, no. 10 (2022): 3492–3499, https://doi.org/10.1021/acsenergylett.2c01750.

34. D. Seo, A. Grieder, A. Radmilovic, et al., "Atomic Doping to Enhance the p-Type Behavior of $BiFeO_3$ Photoelectrodes for Solar H_2O_2 Production," *Journal of Materials Chemistry A* 12, no. 31 (2024): 20437–20448, https://doi.org/10.1039/d4ta03191a.

35. K. Tan, Y. Chen, C. Van, et al., "Energy Band Gap Modulation in Nd-Doped $BiFeO_3$/$SrRuO_3$ Heteroepitaxy for Visible Light Photoelectrochemical Activity," *ACS Applied Materials & Interfaces* 11, no. 1 (2019): 1655–1664, https://doi.org/10.1021/acsami.8b17758.

36. M. I. Díez-García and R. Gómez, "Metal Doping to Enhance the Photoelectrochemical Behavior of $LaFeO_3$ Photocathodes," *ChemSusChem* 10, no. 11 (2017): 2457–2463, https://doi.org/10.1002/cssc.201700166.

37. X. Sun, D. Tiwari, and D. J. Fermin, "Promoting Active Electronic States in $LaFeO_3$ Thin-Films Photocathodes via Alkaline-Earth Metal Substitution," *ACS Applied Materials & Interfaces* 12, no. 28 (2020): 31486–31495, https://doi.org/10.1021/acsami.0c08174.

38. A. T. Kozakov, A. G. Kochur, K. A. Googlev, et al., "X-Ray Photoelectron Study of the Valence State of Iron in Iron-Containing Single-Crystal ($BiFeO_3$, $PbFe_{1/2}Nb_{1/2}O_3$), and Ceramic ($BaFe_{1/2}Nb_{1/2}O_3$) Multiferroics," *Journal of Electron Spectroscopy and Related Phenomena* 184 (2011): 16–23, https://doi.org/10.1016/j.elspec.2010.10.004.

39. X. Sun, D. Tiwari, and D. J. Fermin, "High Interfacial Hole-Transfer Efficiency at $GaFeO_3$Thin Film Photoanodes," *Advanced Energy Materials* 10, no. 45 (2020): 2002784, https://doi.org/10.1002/aenm.202002784.

40. X. Sun, D. Tiwari, M. Li, and D. J. Fermin, "Decoupling the Impact of Bulk and Surface Point Defects on the Photoelectrochemical Properties of

$LaFeO_3$ Thin Films," *Chemical Science* 13, no. 37 (2022): 11252–11259, https://doi.org/10.1039/d2sc04675j.

41. G. P. Wheeler, V. U. Baltazar, T. J. Smart, et al., "Combined Theoretical and Experimental Investigations of Atomic Doping To Enhance Photon Absorption and Carrier Transport of $LaFeO_3$ Photocathodes," *Chemistry of Materials* 31, no. 15 (2019): 5890–5899, https://doi.org/10.1021/acs.chemmater.9b02141.

42. X. Sun, Z. Lan, M. Wang, et al., "Multifunctional Role of Ag-Substitution in Enhancing the Photoelectrochemical Properties of $LaFeO_3$ Photocathodes," *Chemsuschem* 16, no. 20 (2023): e202300645, https://doi.org/10.1002/cssc.202300645.

43. Y. Zhu, W. Zhou, J. Yu, et al., "Enhancing Electrocatalytic Activity of Perovskite Oxides by Tuning Cation Deficiency for Oxygen Reduction and Evolution Reactions," *Chemistry of Materials* 28, no. 6 (2016): 1691–1697, https://doi.org/10.1021/acs.chemmater.5b04457.

44. D. Kang, J. C. Hill, Y. Park, and K. S. Choi, "Photoelectrochemical Properties and Photostabilities of High Surface Area $CuBi_2O_4$ and Ag-Doped $CuBi_2O_4$ Photocathodes," *Chemistry of Materials* 28, no. 12 (2016): 4331–4340, https://doi.org/10.1021/acs.chemmater.6b01294.

45. Z. Yuan, S. Zhao, F. H. Liu, et al., "Exploring the Influence of Grain Boundaries on Carrier Transport and PEC Activity of Hematite Photoelectrodes," *ACS Applied Energy Materials* 8, no. 12 (2025): 8579–8588, https://doi.org/10.1021/acsaem.5c01234.

46. M. Kölbach, H. Hempel, K. Harbauer, et al., "Grain Boundaries Limit the Charge Carrier Transport in Pulsed Laser Deposited α-$SnWO_4$ Thin Film Photoabsorbers," *ACS Applied Energy Materials* 3, no. 5 (2020): 4320–4330, https://doi.org/10.1021/acsaem.0c00028.

47. L. Peng, H. Deng, J. Tian, et al., "Influence of Co Doping on Structural, Optical and Magnetic Properties of $BiFeO_3$ Films Deposited on Quartz Substrates by Sol-Gel Method," *Applied Surface Science* 268 (2013): 146–150, https://doi.org/10.1016/j.apsusc.2012.11.176.

48. A. Hankin, F. E. Bedoya-Lora, J. C. Alexander, A. Regoutz, and G. H. Kelsall, "Flat Band Potential Determination: Avoiding the Pitfalls," *Journal of Materials Chemistry A* 7, no. 45 (2019): 26162–26176, https://doi.org/10.1039/c9ta09569a.

49. X. Sun, M. Wang, Q. Geng, et al., "Nanostructured $AlFeO_3$ Thin Films as a Novel Photoanode for Photoelectrochemical Water Splitting," *Nano Research* 17, no. 3 (2024): 1075–1085, https://doi.org/10.1007/s12274-023-5896-3.

50. X. Sun, D. Tiwari, and D. J. Fermin, "Nanostructured $LaFeO_3$ Photocathodes with Onset Potentials for the Hydrogen Evolution Reaction Over 1.4 V vs. RHE," *Journal of the Electrochemical Society* 166, no. 15 (2019): H764, https://doi.org/10.1149/2.0141915jes.

51. M. G. Walter, E. L. Warren, J. R. McKone, et al., "Solar Water Splitting Cells," *Chemical Reviews* 110, no. 11 (2010): 6446–6473, https://doi.org/10.1021/cr1002326.

Supporting Information

Additional supporting information can be found online in the Supporting Information section. **Supporting Fig. S1:** Valence band spectra of pristine and 6% Ag-doped BFO films obtained from XPS measurement. **Supporting Fig. S2:** Equivalent Tauc plots obtained from the EQE spectra in Figure 5c: (a) pristine BFO films; (b) 6% Ag-doped BFO films. The corresponding fitting results reveal a band gap of 2.69 eV and 2.56 eV for pristine and 6% Ag-doped BFO films, respectively, which is highly consistent with the values estimated from the UV-vis absorption spectra in Figure 4a. **Supporting Fig. S3:** Photocurrent-time plots of pristine and 6% Ag-doped BFO films in 0.1 M Na_2SO_4 aqueous solutions (pH 12) at 0.5 V vs RHE. **Supporting Table S1:** Rietveld refinement results and correlation parameters.**Supporting Table S2:** Fe species contents in pristine and 6% Ag-doped BFO films obtained through the deconvolution of Fe $2p_{3/2}$ peaks in Figure 2. **Supporting Table S3:** Comparison of photocurrent density for various BFO photocathodes under AM 1.5G illumination ($100\ mW{\cdot}cm^{-2}$).